ADVANCED MATERIALS
www.advmat.de

Heterogeneous Electronic and Photonic Devices Based on Monolayer Ternary Telluride Core/Shell Structures

*Kai Xu, Ankit Sharma, Junzhe Kang, Xiaoqiao Hu, Zheng Hao, and Wenjuan Zhu**

Device engineering based on the tunable electronic properties of ternary transition metal dichalcogenides has recently gained widespread research interest. In this work, monolayer ternary telluride core/shell structures are synthesized using a one-step chemical vapor deposition process with rapid cooling. The core region is the tellurium-rich $WSe_{2-2x}Te_{2x}$ alloy, while the shell is the tellurium-poor $WSe_{2-2y}Te_{2y}$ alloy. The bandgap of the material is ≈1.45 eV in the core region and ≈1.57 eV in the shell region. The lateral gradient of the bandgap across the monolayer heterostructure allows for the fabrication of heterogeneous transistors and photodetectors. The difference in work function between the core and shell regions leads to a built-in electric field at the heterojunction. As a result, heterogeneous transistors demonstrate a unidirectional conduction and strong photovoltaic effect. The bandgap gradient and high mobility of the ternary telluride core/shell structures provide a unique material platform for novel electronic and photonic devices.

Alloying in 2D transition metal dichalcogenides (TMDs) has allowed bandgap engineering and phase transformation, which enables a new series of electronic and photonic devices. Bandgap engineering has been demonstrated in various TMD ternary alloys, including $MoS_{2(1-x)}Se_{2x}$,[1–6] $WS_{2(1-x)}Se_{2x}$,[7,8] $Mo_{1-x}W_xS_2$,[9–13] and $Mo_{1-x}W_xSe_2$[14,15] by adjusting the composition of the elements. A 2H-1T' phase transformation was observed in $Mo_{1-x}Re_xSe_2$.[16] Furthermore, the carrier polarity can be modulated between n- and p-type by tuning the alloy composition in $WS_{2(1-x)}Se_{2x}$ and $Mo_{1-x}W_xSe_2$ transistors.[17,18] However, these alloys are mainly based on sulfide and selenide, in which the bandgap range is limited to 1.57–2.03 eV. To further expand the bandgap range, tellurium-based alloys are needed. For example, WTe_2 is a semimetal,[19,20] while monolayer WSe_2 is a semiconductor with wide bandgap (≈1.64 eV).[21–23] The bandgap of ternary alloy $WSe_{2-2x}Te_{2x}$ can potentially be tunable from 0 to 1.64 eV, covering a broad range of the electromagnetic spectrum from infrared (IR) to visible light. Furthermore, telluride-based alloys have a rich variety of structure phases.[24–26] For example, telluride-based $WSe_{2-2x}Te_{2x}$ alloy is 2H semiconducting phase with $0 < x < 0.5$ and $1T_d$ metallic phase with $0.6 < x < 1$.[27]

Dr. K. Xu, A. Sharma, J. Kang, X. Hu, Z. Hao, Prof. W. Zhu
Electrical and Computer Engineering
University of Illinois at Urbana-Champaign
Urbana, IL 61801, USA
E-mail: wjzhu@illinois.edu

The ORCID identification number(s) for the author(s) of this article can be found under https://doi.org/10.1002/adma.202002548.

DOI: 10.1002/adma.202002548

However, the synthesis of tellurium alloy is very challenging due to the low activity of tellurium and poor thermal stability of tellurium alloy.[28] In the past, $WSe_{2-2x}Te_{2x}$ alloys were synthesized using chemical vapor transport (CVT).[27] However, CVT is time-consuming and the flakes obtained by the exfoliation of the CVT crystal are random in size and thickness, imposing a severe limitation on commercialization. In contrast, chemical vapor deposition (CVD) synthesis provides much better control on the crystal thickness and is more promising for large-scale production. Recently, it was reported that tellurium alloys can be synthesized using CVD as well, including hydrogen-assisted post-growth substitution of tellurium into MoS_2,[29] growing $MoSe_{2(1-x)}Te_{2x}$ alloys using sodium cholate,[30] tellurizing MoS_2 and WS_2 via alkali metal scooter,[28] and synthesizing $WTe_2S_{2(1-x)}$ using sodium chloride.[31] However, the ternary telluride heterostructures and their electronic and photonic devices remain unexplored.

In this work, monolayer $WSe_{2-2x}Te_{2x}/WSe_{2-2y}Te_{2y}$ core/shell structures were synthesized via a one-step CVD method with rapid cooling. Here the tellurium concentration is high in the core and low in the shell regions, that is, $x > y$. The electronic devices based on $WSe_{2-2x}Te_{2x}/WSe_{2-2y}Te_{2y}$ heterostructures exhibit polarity modulation and high mobility. Interestingly, the bandgap difference at the core and shell regions leads to unidirectional transport and prominent photovoltaic effect. Our research work provides a foundation for the synthesis of 2D TMDC alloys with core/shell structures and opens new and exciting opportunities for tailoring multifunctional electronic and optoelectronic devices based on ternary TMDCs.

Rapid cooling in CVD has been shown to aid in the formation of TMDC crystals and to preserve metastable states.[32–35] In this work, we use rapid cooling to form the $WSe_{2-2x}Te_{2x}/WSe_{2-2y}Te_{2y}$ core/shell structures. The schematic for the experimental setup is shown in Figure S1, Supporting Information. Following the formation of an unstable $WSe_{2-2x}Te_{2x}$ nucleation during the growth process, adjusting the cooling rate results in two possible outcomes, seen in the schematic in **Figure 1**a. A homogeneous WSe_2 crystal is formed using natural cooling process, while $WSe_{2-2x}Te_{2x}/WSe_{2-2y}Te_{2y}$ core/shell structures are formed using rapid cooling process, as shown in Figure 1b. A homemade water-based system was capable of rapidly cooling the furnace at about 20 °C min^{-1}, discussed further in the Supporting Information. Figure 1c,d shows the outcomes of growth conducted without and with the water-based rapid-cooling

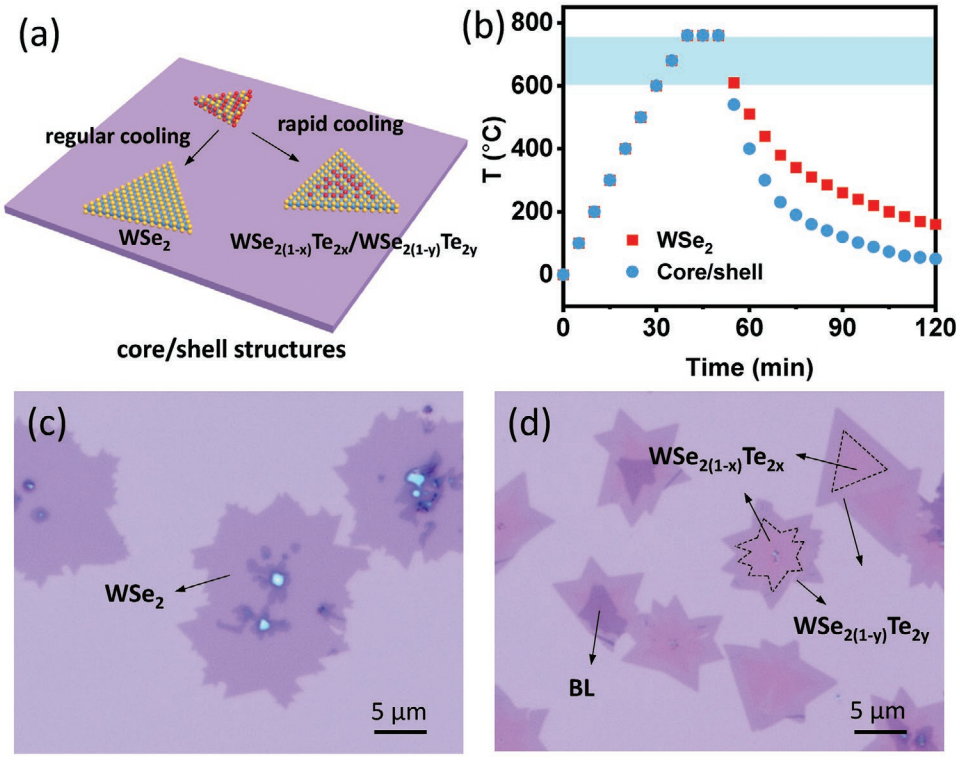

Figure 1. Synthesis of monolayer $WSe_{2-2x}Te_{2x}/WSe_{2-2y}Te_{2y}$ core/shell heterostructures using one-step CVD. a) The schematic of the growth process. Two possible outcomes can be expected following the formation of an unstable $WSe_{2-2x}Te_{2x}$ nucleation. A homogeneous WSe_2 crystal is formed using natural cooling process, while $WSe_{2-2x}Te_{2x}/WSe_{2-2y}Te_{2y}$ core/shell structures are formed using rapid cooling process. b) The temperature ramp profiles for WSe_2 and $WSe_{2-2x}Te_{2x}/WSe_{2-2y}Te_{2y}$ core/shell growth. c,d) Optical images of WSe_2 (c) and $WSe_{2-2x}Te_{2x}/WSe_{2-2y}Te_{2y}$ core/shell heterostructures (d).

system, respectively. Without rapid cooling, only pure WSe_2 appears, the energetically favorable case. Rapid cooling prevents excess selenium from exchanging with the less-reactive tellurium during the cooling phase of the growth process. As a result, $WSe_{2-2x}Te_{2x}/WSe_{2-2y}Te_{2y}$ core/shell structures were formed, shown in Figure 1d.

Figure 2 summarizes our characterizations of the CVD-grown monolayer $WSe_{2-2x}Te_{2x}/WSe_{2-2y}Te_{2y}$ core/shell structures. The CVD process with rapid cooling usually resulted in high-quality star-shaped crystals with a dark center region. We conducted Raman and photoluminescence (PL) measurements on the monolayers using a Renishaw confocal Raman microscope. A comparison of PL measurements from the core and shell regions of the lateral heterostructure is shown in Figure 2a. The PLs taken in the core and shell regions show peaks at 1.45 and 1.57 eV, respectively, which indicates that the tellurium concentration in the core region is higher than that in the shell region. The Raman spectra of the two regions further confirm the presence of tellurium as shown in Figure 2b. As expected, the Raman spectrum taken in the shell region shows a peak at 243 cm^{-1} corresponding to the E^1_{2g} mode and a peak at 253 cm^{-1} corresponding to the A_{1g} mode in monolayer WSe_2. The Raman spectrum taken in the core region shows that the peak corresponding to the E^1_{2g} mode redshifts while the A_{1g} peak is greatly diminished, which is consistent with the results obtained on exfoliated $WSe_{2-2x}Te_{2x}$ flakes.[27] PL mapping of the flake is shown in Figure 2c to better illustrate the $WSe_{2-2x}Te_{2x}$ and $WSe_{2-2y}Te_{2y}$ regions of the heterostructure. The image reveals that the core region is largely homogeneous. The thickness of the lateral heterostructure is confirmed with atomic force microscopy (AFM), as shown in Figure 2d. The thickness of the flake is about 1.1 nm. The flat morphology of the $WSe_{2-2x}Te_{2x}$ alloy can be seen in the AFM image as well as the height profile, confirming the presence of monolayer $WSe_{2-2x}Te_{2x}/WSe_{2-2y}Te_{2y}$ core/shell structures. To characterize the crystal structure and chemical composition directly, our samples were measured using atomic-resolution scanning transmission electron microscopy (STEM) and energy-dispersive X-ray spectroscopy (EDS). Figure 2e shows a high-angle annular dark-field (HAADF) image of the $WSe_{2-2x}Te_{2x}$ alloy. 2H crystal structure is clearly observed. A high-magnification HAADF image of the alloy is shown in Figure 2f, where the W, 2Te, SeTe, 2Se, and Se sites are identified according to the intensity. Tellurium compositions of 2.4% and 10.9% for the shell and core regions were obtained based on EDS measurements as shown in Figure S2, Supporting Information.

Utilizing the synthesized monolayer telluride heterostructures, we fabricated homogeneous core ($WSe_{2-2x}Te_{2x}$) and shell ($WSe_{2-2y}Te_{2y}$) transistors side-by-side within a single flake, as shown in **Figure 3**a. For comparison, the channels of the transistors were patterned into rectangular shape using e-beam lithography and oxygen plasma etch. The channel length is 2 μm and channel width is 1 μm for all transistors. The shell transistor shows strong p-type transport, while the core transistor displays ambipolar transport (Figure 3b). This phenomenon can be explained by the bandgap difference between these

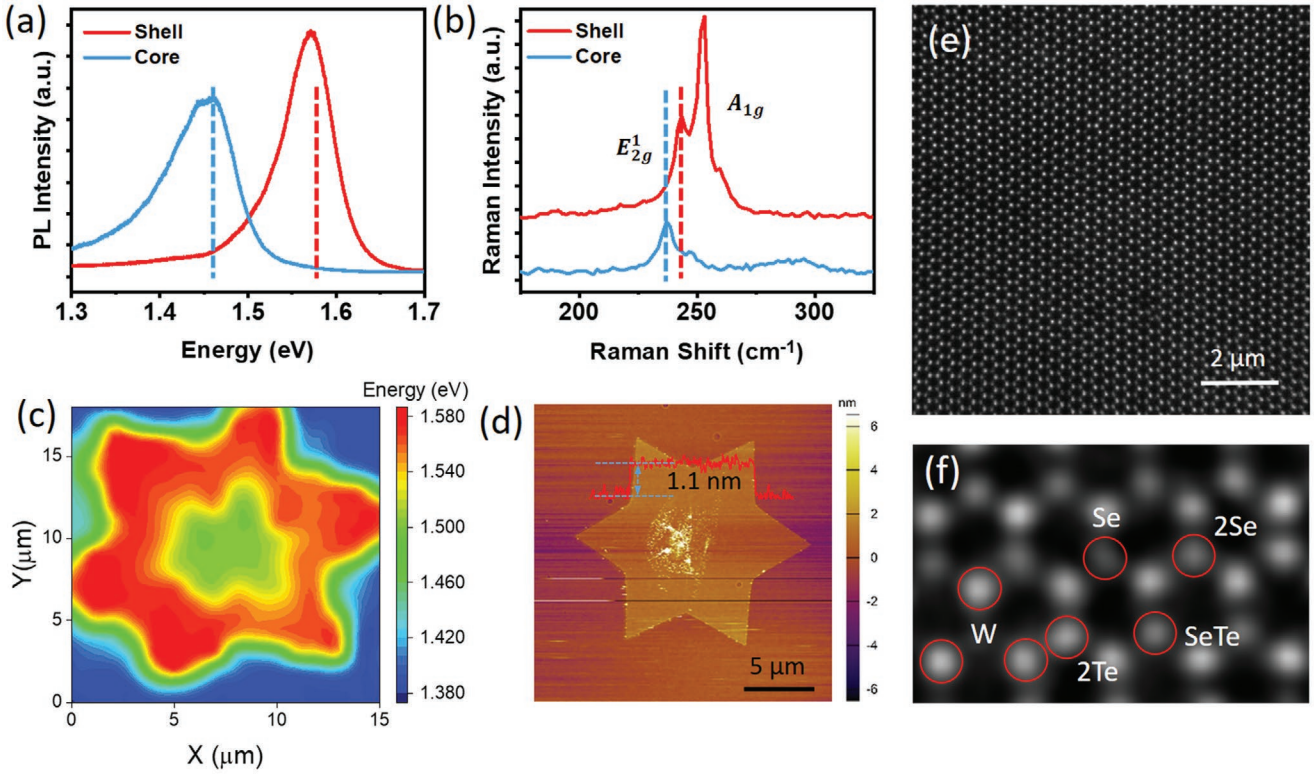

Figure 2. Characterization of the monolayer $WSe_{2-2x}Te_{2x}/WSe_{2-2y}Te_{2y}$ core/shell heterostructures grown by CVD. a) PL spectra taken in the core ($WSe_{2-2x}Te_{2x}$) and shell ($WSe_{2-2y}Te_{2y}$) regions of the lateral heterostructures. The peak of the PL taken in the shell region is located at 1.57 eV, which is similar to monolayer WSe_2, while the peak of the PL taken in the core region is located at 1.45 eV, corresponding to the $WSe_{2-2x}Te_{2x}$. b) Raman spectra taken in the core ($WSe_{2-2x}Te_{2x}$) and shell ($WSe_{2-2y}Te_{2y}$) regions of the heterostructure. c) PL mapping reveals that the core region is largely homogeneous. d) AFM measurement confirms the monolayer nature of the heterostructure. e) Low- and high-magnification HAADF images of ternary telluride alloy grown by CVD. 2H crystal structure is observed clearly.

two materials, which will be discussed later. The hole field-effect mobilities of the telluride in the core and shell regions are 14 and 0.12 $cm^2\ V^{-1}\ s^{-1}$, respectively. The statistical distribution of the hole mobilities of the telluride in the shell region is shown in Figure S4, Supporting Information, which reveals that the mobility ranges from 2 to 30 $cm^2\ V^{-1}\ s^{-1}$ with a mean of 10 $cm^2\ V^{-1}\ s^{-1}$. The values are comparable to those of CVD-grown WSe_2 in previous reports.[36–38] The average of the hole mobility of the telluride in the core region is about 2 $cm^2\ V^{-1}\ s^{-1}$. Furthermore, the temperature-dependent mobilities of the telluride in the shell region were extracted from transfer curves, shown in Figure 3c. In the high-temperature regime above 150 K, the hole mobility decreases with increasing temperature due to phonon scattering. The temperature dependence of the hole mobility can be fitted as $\mu \sim T^{-\gamma}$, where γ is about 1.3. To further evaluate the electrical properties, we characterized the temperature dependence of the transfer curves for homogeneous transistors in the core and shell regions (Figure S5, Supporting Information). The effective Schottky barriers were extracted using the equation: $I_d = AA^*T^2 \exp\left(-\frac{\Phi_{SB}}{kT}\right)$, where A is the junction area, A^* is the Richardson constant, Φ_{SB} is the Schottky barrier height, k is the Boltzmann constant, and T is the temperature.[39] Figure 3d shows the effective Schottky barrier as a function of gate voltage. When the gate voltage is higher than the flatband voltage, thermionic emission of holes over the Schottky barrier dominates the current, so the effective barrier height changes linearly with gate voltage. When the gate voltage is lower than the flatband voltage, tunneling of holes through the Schottky barrier starts to contribute to the current as well, thus the linear dependence of effective barrier height on gate voltage no long prevails. Based on the curves in Figure 3d, we can extract the flatband voltages of these transistors and the Schottky barrier heights at flatband voltages. As compared to the transistor in the shell region, the transistor in the core region shows higher Schottky barrier for holes, that is, the Fermi level of the contact metal (Pd) is further away from the valence band of the core $WSe_{2-2y}Te_{2y}$. Furthermore, spectral photocurrent measurement of the core and shell phototransistors confirms the impact of tellurium incorporation on the bandgap, as shown in Figure 3e. The photoresponsivity is calculated using the equation: $R = I_{ph}/P$, where I_{ph} is the photocurrent. P is the effective laser power irradiated on device, which is calculated using $P = I \times A$, where I is the laser intensity and A is the device area. The spectral photoresponsivity curves for the core and shell phototransistors display three peaks, corresponding to the A, B, and Á excitons, respectively. Here, the ground state A exciton and the spin–orbit (SO) split B exciton are associated with the K-point of the Brillouin zone, while the Á exciton is the excited state of the A exciton.[40,41] The

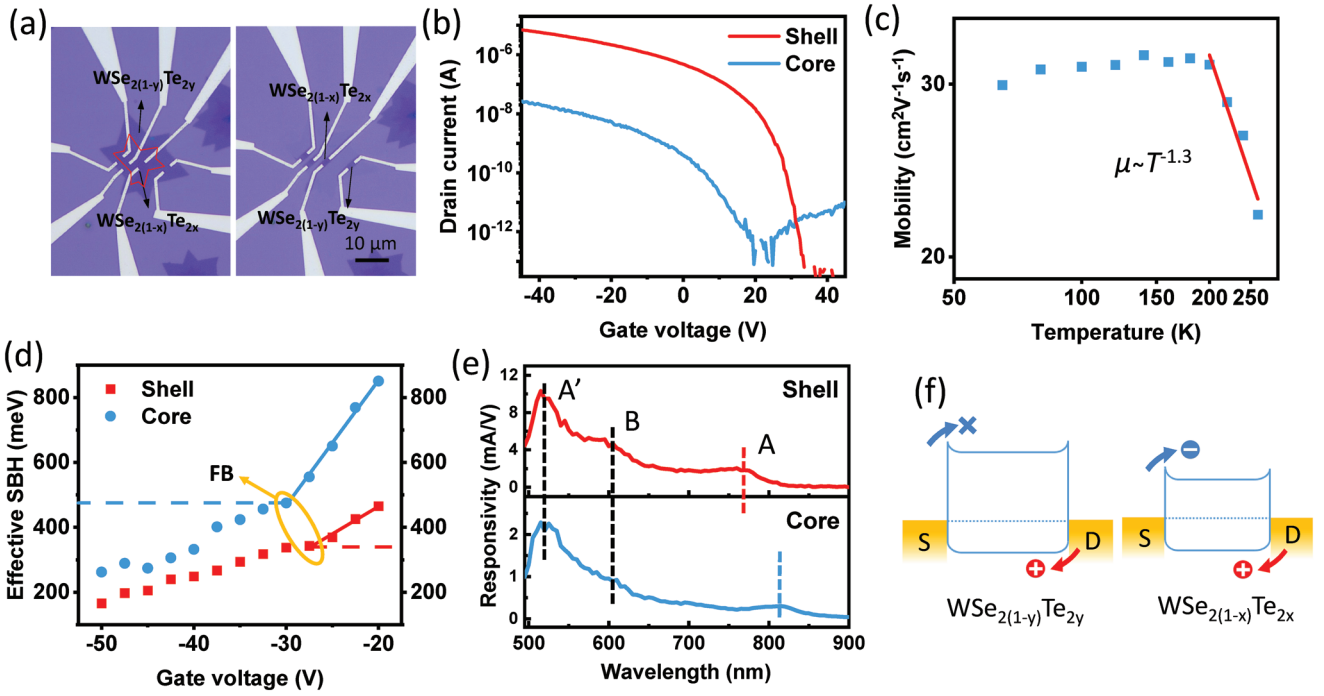

Figure 3. Electrical characterization of homogeneous core ($WSe_{2-2x}Te_{2x}$) and shell ($WSe_{2-2y}Te_{2y}$) transistors. a) Optical image of the transistors. b) The homogeneous shell transistor shows strong p-type transport, while the core transistor displays ambipolar behavior. The difference between the core and shell regions can be attributed to the bandgap difference between these two materials. c) Temperature-dependence of hole motilities in a homogeneous shell transistor. d) Effective Schottky barrier height as a function of gate voltage for shell and core transistors. e) Spectral photoresponsivity of the homogeneous shell and core transistors reveals three exciton peaks. The A exciton peak in core $WSe_{2-2x}Te_{2x}$ redshifts as compared to that in shell $WSe_{2-2y}Te_{2y}$, indicating that tellurium incorporation in the film reduces the bandgap. f) Band alignments of core and shell transistors along the channel. The shell $WSe_{2-2y}Te_{2y}$ transistor has smaller hole Schottky barrier, which facilitates hole transport, while the core $WSe_{2-2x}Te_{2x}$ has more balanced electron/hole Schottky barriers, favoring ambipolar transport.

shift of the A exciton peak between the core and shell telluride indicates a bandgap change, which also corresponds well to the PL spectra in Figure 2b. Combining the Schottky barrier heights extracted from the IVs and the bandgaps measured using PLs and spectral photocurrent, we can construct the energy diagram of homogeneous core and shell transistors, shown in Figure 3f. The band alignment between the core $WSe_{2-2x}Te_{2x}$ and Pd enables simultaneous transport of both electrons and holes, which explains the ambipolar transport in the core $WSe_{2-2x}Te_{2x}$ transistor in Figure 3b. In the shell $WSe_{2-2y}Te_{2y}$/Pd contact, however, the low Schottky barrier for holes facilitates hole transport, while the large Schottky barrier for electrons limits the electron transport, leading to p-type transport shown in Figure 3b.

The bandgap difference between core and shell regions can be used to construct heterogeneous electronic and photonic devices. **Figure 4**a shows the optical images of the heterogeneous $WSe_{2-2x}Te_{2x}$/$WSe_{2-2y}Te_{2y}$ transistors and photodetectors. The hole current in homogeneous shell transistor is much higher than that in core transistor, shown in Figure 4b, which is consistent with Schottky barrier results in Figure 3. Heterogeneous transistors with core/shell hybrid channels show p-type transport and the drain current is higher when the shell is used as drain than that when the core is used as drain. This asymmetric transport is further elucidated in the output characteristics (Figure 4c). The rectifying behavior indicate that the current prefers to flow from the shell to the core. This phenomenon can be explained by the band diagram in the inset of Figure 4c. Since the Schottky barrier for holes at the shell $WSe_{2-2y}Te_{2y}$/Pd contact is smaller than that at the core $WSe_{2-2x}Te_{2x}$/Pd contact, the drain current is higher for positive drain voltage (i.e., holes inject from shell contact) than for negative drain voltage (i.e., holes inject from the core contact). In addition, positive voltage on the shell region provides a forward bias on the core/shell heterojunction, which will also facilitate the carrier transport through the junction, consistent with the unidirectional transport observed in these heterogeneous transistors. The optoelectronic properties of the core/shell heterostructure were also measured. The *I*–*V* curves under laser exposure were measured as shown in Figure 4d. The shift of the *I*–*V* curve under various laser powers clearly indicates that the photovoltaic effect is observed. An open-circuit voltage of 0.48 V and a short-circuit current of 0.17 nA were achieved when a 532 nm laser (power = 5.1 μW) was shined onto the heterostructure. The photovoltaic effect is due to the built-in electric field and band bending at the core/shell heterojunction, which is induced by the different work functions of tellurium-rich and tellurium-poor tellurides. Furthermore, the photocurrents of homogeneous and heterogeneous transistors are compared in Figure S7, Supporting Information. The photoresponsivities extracted at V_D = 1 *V* are 4.1×10^3, 1.11, and 8.4 mA W^{-1} for the shell, core, and core/shell transistors, respectively. The photoresponsivity of the shell $WSe_{2-2y}Te_{2y}$ transistor is significantly higher than that of the

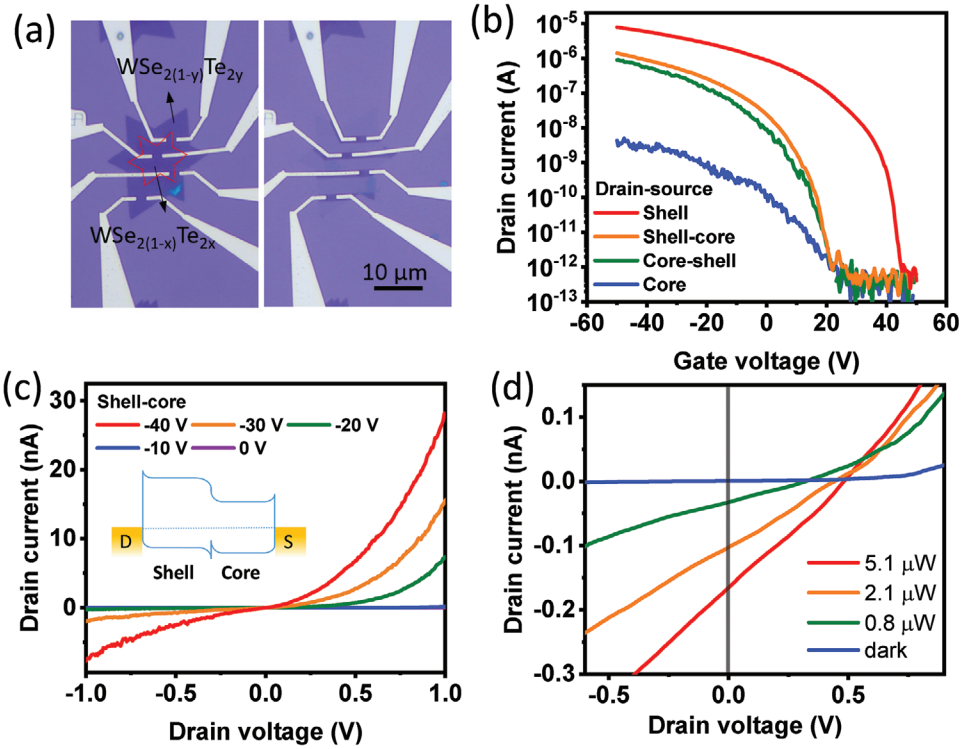

Figure 4. Electrical and optoelectrical characterizations of heterogeneous core/shell transistors. a) Optical image of heterogeneous transistors. b) Transfer curves with homogeneous and heterogeneous transistors with various combinations of channel materials. Drain voltage $V_D = 1$ V. c) Output characteristics of heterogeneous transistors showing rectifying behavior. Inset: The energy diagram of the heterogeneous core/shell transistor. d) The *I–V* curves under laser exposure demonstrate the photovoltaic effect in core/shell lateral heterostructures.

core $WSe_{2-2x}Te_{2x}$ transistor due to the reduced hole Schottky barrier and contact resistance in the shell transistor. Since the contact resistances in TMD transistors are typically much larger than the channel resistances,[42,43] contact resistance plays an important role in the photocurrent and photoresponsivity of the transistors.

In summary, monolayer $WSe_{2-2x}Te_{2x}/WSe_{2-2y}Te_{2y}$ core/shell heterostructures were synthesized using a one-step rapid-cooling CVD method. Rapid cooling can prevent excess selenium from exchanging with tellurium during the cooling step of the growth process and tellurium can be preserved in the core of the flakes. PL and EDS spectra indicate that $WSe_{2-2x}Te_{2x}$ in the core region has high tellurium concentration (small bandgap), while $WSe_{2-2y}Te_{2y}$ in the shell region has low tellurium concentration (large bandgap). AFM confirms the monolayer nature of the core/shell structure. Furthermore, high-performance homogeneous transistors based on telluride in the core and shell regions were fabricated. Shell-based transistors showed unipolar p-type transport, high current on/off ratio (>10^6), and maximum mobility of 30 $cm^2\ V^{-1}\ s^{-1}$. In contrast, core-based transistors displayed ambipolar behavior, which can be explained by the difference in band alignment between these two materials and metal contacts. More importantly, the photovoltaic effect was observed in the heterogeneous core/shell transistors, due to the built-in electric field at the heterojunction. Our findings provide experimental groundwork for the synthesis of core/shell telluride structures and open new opportunities for their application in multifunctional devices.

Experimental Section

Synthesis of Monolayer $WSe_{2-2x}Te_{2x}/WSe_{2-2y}Te_{2y}$ Core/Shell Heterostructures: WO_3 powder was placed in the center of the CVD furnace, and selenium powder and tellurium powder were placed about 8–12 cm upstream from the WO_3. Before the growth, the tube of the furnace was flushed three times using Ar gas and then pumped to below 1 Pa. First, the temperature of the furnace was ramped up to 600 °C, while flowing Ar gas at 90 sccm. Then the temperature was increased from 600 to 760 °C within 10 min, while flowing 90 sccm Ar and 9 sccm H_2 gas. The synthesis was carried out at 760 °C for 10 min. Then the furnace was cooled rapidly using a homemade water-based system at 20 °C min^{-1}.

Material and Device Characterizations: The morphologies and thickness of monolayer $WSe_{2-2x}Te_{2x}/WSe_{2-2y}Te_{2y}$ core/shell heterostructures were characterized by optical microscopy (Olympus BX53M) and atomic force microscopy (Asylum AFM). The Raman spectra and photoluminescence were performed on a confocal-microscope-based Raman spectrometer (Renishaw, 532 nm excitation laser). The crystal structures and chemical compositions were obtained by atomic-revolution scanning tunneling electron microscopy (Thermo Fisher Scientific Themis Z aberration-corrected STEM) and energy-dispersive X-ray spectroscopy (EDS). Electrical properties were measured using a probe station (lakeshore CPX-VF) with a semiconductor device analyzer (Keysight B1500A). The optoelectrical properties were measured in the homemade photocurrent measurement system.

Supporting Information

Supporting Information is available from the Wiley Online Library or from the author.

Acknowledgements

The authors would like to acknowledge the support from the Office of Naval Research (ONR) under Grant NAVY N00014-17-1-2973 and National Science Foundation (NSF) under Grants ECCS 16-53241 CAR.

Conflict of Interest

The authors declare no conflict of interest.

Author Contributions

K.X. and A.S. contributed equally to this work. The manuscript was written through contributions of all authors. All authors have given approval to the final version of the manuscript.

Keywords

core/shell structures, heterogeneous transistors, ternary tellurides

Received: April 14, 2020
Revised: September 11, 2020
Published online:

[1] J. Mann, Q. Ma, P. M. Odenthal, M. Isarraraz, D. Le, E. Preciado, D. Barroso, K. Yamaguchi, G. von Son Palacio, A. Nguyen, T. Tran, M. Wurch, A. Nguyen, V. Klee, S. Bobek, D. Sun, T. F. Heinz, T. S. Rahman, R. Kawakami, L. Bartels, *Adv. Mater.* **2014**, *26*, 1399.
[2] H. Li, X. Duan, X. Wu, X. Zhuang, H. Zhou, Q. Zhang, X. Zhu, W. Hu, P. Ren, P. Guo, L. Ma, X. Fan, X. Wang, J. Xu, A. Pan, X. Duan, *J. Am. Chem. Soc.* **2014**, *136*, 3756.
[3] Q. Feng, N. Mao, J. Wu, H. Xu, C. Wang, J. Zhang, L. Xie, *ACS Nano* **2015**, *9*, 7450.
[4] Q. Feng, Y. Zhu, J. Hong, M. Zhang, W. Duan, N. Mao, J. Wu, H. Xu, F. Dong, F. Lin, C. Jin, C. Wang, J. Zhang, L. Xie, *Adv. Mater.* **2014**, *26*, 2648.
[5] Y. Gong, Z. Liu, A. R. Lupini, G. Shi, J. Lin, S. Najmaei, Z. Lin, A. L. Elías, A. Berkdemir, G. You, H. Terrones, M. Terrones, R. Vajtai, S. T. Pantelides, S. J. Pennycook, J. Lou, W. Zhou, P. M. Ajayan, *Nano Lett.* **2014**, *14*, 442.
[6] H. Li, X. Duan, X. Wu, X. Zhuang, H. Zhou, Q. Zhang, X. Zhu, W. Hu, P. Ren, P. Guo, L. Ma, X. Fan, X. Wang, J. Xu, A. Pan, X. Duan, *J. Am. Chem. Soc.* **2014**, *136*, 3756.
[7] H. Sun, J. Wang, F. Wang, L. Xu, K. Jiang, L. Shang, Z. Hu, J. Chu, *Nanoscale* **2018**, *10*, 11553.
[8] X. Duan, C. Wang, Z. Fan, G. Hao, L. Kou, U. Halim, H. Li, X. Wu, Y. Wang, J. Jiang, A. Pan, Y. Huang, R. Yu, X. Duan, *Nano Lett.* **2016**, *16*, 264.
[9] Y. Kobayashi, S. Mori, Y. Maniwa, Y. Miyata, *Nano Res.* **2015**, *8*, 3261.
[10] J. Park, M. S. Kim, B. Park, S. H. Oh, S. Roy, J. Kim, W. Choi, *ACS Nano* **2018**, *12*, 6301.
[11] T. Livneh, D. O. Dumcenco, I. Pinkas, *J. Raman Spectrosc.* **2017**, *48*, 773.
[12] A. F. Rigosi, H. M. Hill, K. T. Rim, G. W. Flynn, T. F. Heinz, *Phys. Rev. B* **2016**, *94*, 075440.
[13] H. Liu, K. K. A. Antwi, S. Chua, D. Chi, *Nanoscale* **2014**, *6*, 624.
[14] P. Bampoulis, K. Sotthewes, M. H. Siekman, H. J. W. Zandvliet, *ACS Appl. Mater. Interfaces* **2018**, *10*, 13218.
[15] A. Apte, V. Kochat, P. Rajak, A. Krishnamoorthy, P. Manimunda, J. A. Hachtel, J. C. Idrobo, S. A. Syed Amanulla, P. Vashishta, A. Nakano, R. K. Kalia, C. S. Tiwary, P. M. Ajayan, *ACS Nano* **2018**, *12*, 3468.
[16] V. Kochat, A. Apte, J. A. Hachtel, H. Kumazoe, A. Krishnamoorthy, S. Susarla, J. C. Idrobo, F. Shimojo, P. Vashishta, R. Kalia, A. Nakano, C. S. Tiwary, P. M. Ajayan, *Adv. Mater.* **2017**, *29*, 1703754.
[17] X. Li, M.-W. Lin, L. Basile, S. M. Hus, A. A. Puretzky, J. Lee, Y.-C. Kuo, L.-Y. Chang, K. Wang, J. C. Idrobo, A.-P. Li, C.-H. Chen, C. M. Rouleau, D. B. Geohegan, K. Xiao, *Adv. Mater.* **2016**, *28*, 8240.
[18] X. Duan, C. Wang, Z. Fan, G. Hao, L. Kou, U. Halim, H. Li, X. Wu, Y. Wang, J. Jiang, A. Pan, Y. Huang, R. Yu, X. Duan, *Nano Lett.* **2016**, *16*, 264.
[19] Z. Li, Y. Song, S. Tang, *J. Phys.: Condens. Matter* **2020**, *32*, 333001.
[20] L. Wang, I. Gutiérrez-Lezama, C. Barreteau, N. Ubrig, E. Giannini, A. F. Morpurgo, *Nat. Commun.* **2015**, *6*, 8892.
[21] J. Gusakova, X. Wang, L. L. Shiau, A. Krivosheeva, V. Shaposhnikov, V. Borisenko, V. Gusakov, B. K. Tay, *Phys. Status Solidi* **2017**, *214*, 1700218.
[22] W. Shi, M.-L. Lin, Q.-H. Tan, X.-F. Qiao, J. Zhang, P.-H. Tan, *2D Mater.* **2016**, *3*, 025016.
[23] C. Zhou, Y. Zhao, S. Raju, Y. Wang, Z. Lin, M. Chan, Y. Chai, *Adv. Funct. Mater.* **2016**, *26*, 4223.
[24] Y. Wang, J. Xiao, H. Zhu, Y. Li, Y. Alsaid, K. Y. Fong, Y. Zhou, S. Wang, W. Shi, Y. Wang, A. Zettl, E. J. Reed, X. Zhang, *Nature* **2017**, *550*, 487.
[25] D. H. Keum, S. Cho, J. H. Kim, D.-H. Choe, H.-J. Sung, M. Kan, H. Kang, J.-Y. Hwang, S. W. Kim, H. Yang, K. J. Chang, Y. H. Lee, *Nat. Phys.* **2015**, *11*, 482.
[26] S. Cho, S. Kim, J. H. Kim, J. Zhao, J. Seok, D. H. Keum, J. Baik, D. H. Choe, K. J. Chang, K. Suenaga, S. W. Kim, Y. H. Lee, H. Yang, *Science* **2015**, *349*, 625.
[27] P. Yu, J. Lin, L. Sun, Q. L. Le, X. Yu, G. Gao, C.-H. Hsu, D. Wu, T.-R. Chang, Q. Zeng, F. Liu, Q. J. Wang, H.-T. Jeng, H. Lin, A. Trampert, Z. Shen, K. Suenaga, Z. Liu, *Adv. Mater.* **2017**, *29*, 1603991.
[28] S. J. Yun, G. H. Han, H. Kim, D. L. Duong, B. G. Shin, J. Zhao, Q. A. Vu, J. Lee, S. M. Lee, Y. H. Lee, *Nat. Commun.* **2017**, *8*, 2163.
[29] G. Yin, D. Zhu, D. Lv, A. Hashemi, Z. Fei, F. Lin, A. V. Krasheninnikov, Z. Zhang, H.-P. Komsa, C. Jin, *Nanotechnology* **2018**, *29*, 145603.
[30] A. Apte, A. Krishnamoorthy, J. A. Hachtel, S. Susarla, J. C. Idrobo, A. Nakano, R. K. Kalia, P. Vashishta, C. S. Tiwary, P. M. Ajayan, *Chem. Mater.* **2018**, *30*, 7262.
[31] B. Tang, J. Zhou, P. Sun, X. Wang, L. Bai, J. Dan, J. Yang, K. Zhou, X. Zhao, S. J. Pennycook, Z. Liu, *Adv. Mater.* **2019**, *31*, 1900862.
[32] K. Chen, X. Wan, J. Wen, W. Xie, Z. Kang, X. Zeng, H. Chen, J.-B. Xu, *ACS Nano* **2015**, *9*, 9868.
[33] M. S. Sokolikova, P. C. Sherrell, P. Palczynski, V. L. Bemmer, C. Mattevi, *Nat. Commun.* **2019**, *10*, 712.
[34] C. Li, Y. Yamaguchi, T. Kaneko, T. Kato, *Appl. Phys. Express* **2017**, *10*, 075201.
[35] S. Kang, S. Xia, Z. Zhao, A. Sharma, W. Zhu, in *49th IEEE Semiconductor Interface Specialists Conf.*, IEEE, Piscataway, NJ, USA **2018**.
[36] L. Chen, B. L. Liu, A. N. Abbas, Y. Q. Ma, X. Fang, Y. H. Liu, C. W. Zhou, *ACS Nano* **2014**, *8*, 11543.
[37] J.-K. Huang, J. Pu, C.-L. Hsu, M.-H. Chiu, Z.-Y. Juang, Y.-H. Chang, W.-H. Chang, Y. Iwasa, T. Takenobu, L.-J. Li, *ACS Nano* **2014**, *8*, 923.
[38] Z. H. Yao, J. L. Liu, K. Xu, E. K. C. Chow, W. J. Zhu, *Sci. Rep.* **2018**, *8*, 5221.
[39] Y. Liu, J. Guo, E. Zhu, L. Liao, S.-J. Lee, M. Ding, I. Shakir, V. Gambin, Y. Huang, X. Duan, *Nature* **2018**, *557*, 696.
[40] W. J. Zhao, Z. Ghorannevis, L. Q. Chu, M. L. Toh, C. Kloc, P. H. Tan, G. Eda, *ACS Nano* **2013**, *7*, 791.
[41] A. Arora, M. Koperski, K. Nogajewski, J. Marcus, C. Faugeras, M. Potemski, *Nanoscale* **2015**, *7*, 10421.
[42] W. Liu, D. Sarkar, J. H. Kang, W. Cao, K. Banerjee, *ACS Nano* **2015**, *9*, 7904.
[43] A. Allain, A. Kis, *ACS Nano* **2014**, *8*, 7180.

